

# Evolution of ultra-flat band in van der Waals kagome semiconductor $\text{Pd}_3\text{P}_2(\text{S}_{1-x}\text{Se}_x)_8$

Shaohua Yan<sup>1,†</sup>, Ben-Chao Gong<sup>1,†</sup>, Lin Wang<sup>2</sup>, Jinzhi Wu<sup>1</sup>, Qiangwei Yin<sup>1</sup>, Xinyu Cao<sup>3</sup>, Xiao Zhang<sup>3</sup>, Xiaofeng Liu<sup>2,\*</sup>, Zhong-Yi Lu<sup>1</sup>, Kai Liu<sup>1,\*</sup>, and Hechang Lei<sup>1,\*</sup>

<sup>1</sup>*Department of Physics and Beijing Key Laboratory of Opto-electronic Functional Materials & Micro-nano Devices, Renmin University of China, Beijing 100872, China*

<sup>2</sup>*School of Materials Science & Engineering, Zhejiang University, Hangzhou 310027, China*

<sup>3</sup>*State Key Laboratory of Information Photonics and Optical Communications & School of Science, Beijing University of Posts and Telecommunications, Beijing 100876, China*

(Dated: November 23, 2021)

We investigate the evolutions of structural parameters, optical properties, and electronic structures of van der Waals kagome semiconductor  $\text{Pd}_3\text{P}_2\text{S}_8$  with Se doping. When the doping level of Se increases, the bandgaps of  $\text{Pd}_3\text{P}_2(\text{S}_{1-x}\text{Se}_x)_8$  single crystals decrease gradually, accompanying with the expanded unit cells. The first-principles calculations show that there is a flat band (FB) near the Fermi level in bulk  $\text{Pd}_3\text{P}_2\text{S}_8$ . This FB mainly originates from the  $d_{z^2}$ -like orbitals of Pd atoms in the Pd kagome lattice, which has a finite interlayer electron hopping perpendicular to the  $\text{PdS}_4$  square plane. The interlayer hopping can be reinforced with the Se doping, inducing a stronger interlayer coupling via the chalcogen atoms at apical sites, which reduces the bandgap and enhances the cleavage energy. In contrast, the vanishing interlayer hopping in the two-dimensional limit results in the formation of ultra-FB in the monolayers of these compounds. The easy exfoliation and the existence of unique ultra-FB near  $E_F$  make  $\text{Pd}_3\text{P}_2(\text{S}_{1-x}\text{Se}_x)_8$  a model system to explore the exotic physics of FB in 2D kagome lattice.

Flat band (FB) represents one type of unusual band structure with constant energy independent of the crystal momentum (dispersionless band in momentum space) [1–3]. The zero band width of ideal FB leads to high density of states (DOS) and vanishing group velocity with infinite effective mass of electrons. For the quenched kinetic energy and high DOS, the FB systems are thought to have a strong electron-electron correlation effect naturally, which could cause many of exotic many-body phenomena, like ferromagnetism, superconductivity, Wigner crystals etc [4–9]. Moreover, when time reversal symmetry is broken and spin-orbital coupling is considered, the FB can become topologically nontrivial with non-zero Chern invariant, leading to quantum Hall state or even high-temperature fractional quantum Hall state [10, 11]. In theory, various two-dimensional (2D) lattice models have been proposed to host the FB based on line-graph construction in general [4, 12, 13], such as dice, Lieb, kagome, and decorated square lattices, as well as honeycomb lattice with multiple orbitals on each site [1, 3, 5, 8, 11–18].

The 2D kagome lattice composed of corner-sharing triangles and hexagons of atoms is one of lattice models in which the FB exists [3]. This FB roots in the destructive phase interference of electron hopping paths and in real space the electronic state is geometrically confined within the single hexagon, forming a compact localized state [1, 2]. Theoretical studies have shown that most of exotic phenomena originating from the FB can appear in kagome lattice [4, 7, 8, 10, 11]. Moreover, 2D kagome lattice also exhibits unique topological band structure and strong magnetic frustration effects like topologically nontrivial Dirac band, saddle point with van Hove singularity, quantum spin liquid state [19–23]. Recent experi-

mental studies on insulating or metallic materials with 2D kagome lattice (kagome materials) have confirmed the existence of topological electronic structures including FB [23–27], and revealed various exotic phenomena-fractionalized excitations of spin liquid state, negative FB magnetism, large intrinsic anomalous Hall effect, massive Dirac point with Chern gap, coexisted charge density wave and superconducting states, to name a few [28–37].

Despite a lot of fascinating properties of kagome materials, the experimental studies on their intrinsic physical properties in 2D limit especially for FB are still scarce. Due to the finite interlayer couplings and the existence of structural layers other than the kagome one in real materials, the FB will be perturbed, inducing the band dispersion and hybridization with other bands [24–27]. Thus, in order to reveal the peculiar properties of FB in kagome lattice, the exploration of kagome materials with vanishing interlayer coupling becomes utterly important.

Recently, semiconducting  $\text{Pd}_3\text{P}_2\text{S}_8$  with Pd kagome lattice is highlighted due to its weak van der Waals (vdW) interlayer interaction and feasibility of exfoliation down to monolayer [38]. More interestingly, theoretical calculations show that there is a FB near  $E_F$  with a very small band width in bulk  $\text{Pd}_3\text{P}_2\text{S}_8$ , closely related to the kagome structure of Pd atoms [38], and when the thickness is reduced to monolayer, the dispersion of FB becomes even smaller, i.e., an ultra-FB appears in this material [38]. In order to understand the evolution and origin of this unusual FB in  $\text{Pd}_3\text{P}_2\text{S}_8$ , in this work, we carry out a systematic study on  $\text{Pd}_3\text{P}_2(\text{S}_{1-x}\text{Se}_x)_8$  single crystals with  $x$  up to 0.25. It is found that with Se doping the lattice parameters increase gradually but the bandgaps decrease. Theoretical calculations indicate that the narrowing of bandgap and the increased cleav-

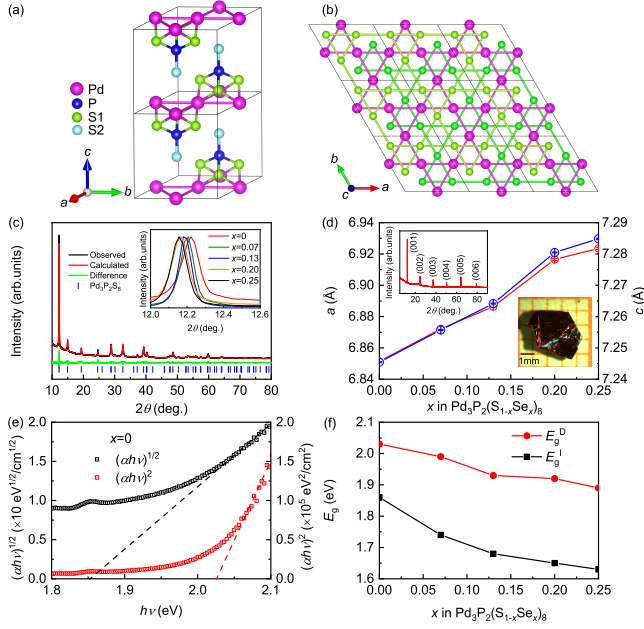


FIG. 1. (a) Crystal structure of  $\text{Pd}_3\text{P}_2\text{S}_8$ . (b) Top view of Pd and S kagome layers. For clarity, the S1 atoms below and above the Pd layer are displayed in different colors. (c) Powder x-ray diffraction (XRD) pattern of  $\text{Pd}_3\text{P}_2\text{S}_8$ . Inset: (00l) diffraction peaks for  $\text{Pd}_3\text{P}_2(\text{S}_{1-x}\text{Se}_x)_8$  with various  $x$ . (d) The  $a$ - and  $c$ -axial lattice parameters  $a$  and  $c$  as a function of  $x$ . Inset: (Left) XRD pattern and (Right) optical photo of a  $\text{Pd}_3\text{P}_2\text{S}_8$  single crystal. (e) The plots of  $(\alpha h\nu)^{1/2}$  and  $(\alpha h\nu)^2$  as a function of  $h\nu$  for  $\text{Pd}_3\text{P}_2\text{S}_8$  single crystal. (f) The estimated direct and indirect bandgaps  $E_g^D$  and  $E_g^I$  of  $\text{Pd}_3\text{P}_2(\text{S}_{1-x}\text{Se}_x)_8$  single crystals with various  $x$ .

age energy can be ascribed to the enhanced interlayer coupling by Se doping. Further analysis reveals that the ultra-FB in monolayer  $\text{Pd}_3\text{P}_2\text{Ch}_8$  ( $\text{Ch} = \text{S}, \text{Se}$ ) originates from the Pd  $d_{z^2}$ -like orbitals of the Pd kagome lattice and the absence of interlayer electron hopping perpendicular to the local  $\text{PdCh}_4$  square plane.

$\text{Pd}_3\text{P}_2\text{S}_8$  has a layered structure with the stacking Pd-P-S blocking layers along the  $c$  axis [Fig. 1(a)]. The key structural ingredient is the perfect Pd kagome lattice in the Pd-P-S layer with the atomic distance of Pd atoms  $d_{\text{Pd-Pd}} \sim 3.418$  Å [Fig. 1(b)] [39, 40]. Below and above the Pd kagome layer, P and S atoms form  $\text{PS}_4$  tetrahedra and each P atom occupies the centre of a tetrahedron. As shown in Fig. 1(a), because of inequivalent local environment of S atoms, there are two S sites and each of three S atoms at S1 site in  $\text{PS}_4$  tetrahedra is coordinated with two Pd atoms and one P atom with  $d_{\text{Pd-S}} \sim 3.113$  Å and  $d_{\text{P-S}} \sim 2.112$  Å, when the fourth S atom at S2 site is coordinated with one P atom only with  $d_{\text{P-S}} \sim 1.904$  Å. Thus, the  $\text{PS}_4$  tetrahedron is distorted with the S-P-S angles deviating from  $109.47^\circ$  in an ideal tetrahedron to  $103.10^\circ$  and  $115.27^\circ$  [39, 40]. More importantly, the vertical P-S bonds in two Pd-P-S layers protrude each other

and it leads to the waved Pd-P-S layers and a unique interlocked layered structure of  $\text{Pd}_3\text{P}_2\text{S}_8$ , different from conventional vdW materials. In addition, in each Pd-P-S layer, the S atoms at S1 site also form two distorted kagome lattices below and above the Pd kagome layer with two different values of  $d_{\text{S-S}}$  ( $\sim 3.176$  Å and  $3.665$  Å) [Fig. 1(b)]. On the other hand, each Pd atom is surrounded with four S atoms from two  $\text{PS}_4$  tetrahedra, forming a  $\text{PdS}_4$  tetragon which tilts away from the  $ab$  plane. In order to keep electric neutrality, the oxidation state of Pd, P, and S in  $\text{Pd}_3\text{P}_2\text{S}_8$  is +2, +5, and -2, respectively. The  $\text{Pd}^{2+}$  ion has an electronic configuration of  $[\text{Kr}]4d^8$ , which usually prefers to have a square-planar crystal field with low spin state. This is consistent with the structural feature and diamagnetism of  $\text{Pd}_3\text{P}_2\text{S}_8$  [38].

Figure 1(c) shows the powder x-ray diffraction (XRD) pattern and Rietveld fit of ground  $\text{Pd}_3\text{P}_2\text{S}_8$  single crystals grown using the self-flux method [41]. The fitted  $a$ - and  $c$ -axial lattice parameters  $a$  and  $c$  are  $6.851(3)$  Å and  $7.246(5)$  Å, close to the previous results [39, 40]. Powder XRD patterns of all Se-doped  $\text{Pd}_3\text{P}_2\text{S}_8$  samples can also be fitted very well by using the crystal structure of  $\text{Pd}_3\text{P}_2\text{S}_8$  with the trigonal symmetry (space group  $P\bar{3}m1$ , No. 164). Both fitted  $a$  and  $c$  increase with increasing Se content monotonically [Fig. 1(d)], which can be ascribed to the larger ionic radius of  $\text{Se}^{2-}$  than  $\text{S}^{2-}$ . The nearly linear trend of lattice expansion follows the Vegard's law. Such increases of lattice parameters are also partially reflected by the shift of peak position of (00l) to lower angle gradually with Se doping [inset of Fig. 1(c)]. It is noted that when  $x > 0.25$ , Se can not be doped into sample further even the nominal  $x$  reaches 0.5 and  $\text{Pd}(\text{S}, \text{Se})_2$  crystals start to grow. This suggests that the solubility limit of Se may be  $x = 0.25$ . The upper left inset of Fig. 1(d) shows the XRD pattern of a  $\text{Pd}_3\text{P}_2\text{S}_8$  single crystal. All of peaks can be indexed by the indices of (00l) lattice planes, indicating that the crystal surface is parallel to the  $ab$  plane and perpendicular to the  $c$  axis. The morphology of  $\text{Pd}_3\text{P}_2\text{S}_8$  single crystal is a thick plate with hexagonal shape [lower right inset of Fig. 1(d)], consistent with the layered structure and the trigonal symmetry of  $\text{Pd}_3\text{P}_2\text{S}_8$ .

Optical transmittance spectra are measured to determine the bandgaps of  $\text{Pd}_3\text{P}_2\text{Ch}_8$  using the Tauc plot method [50]. As shown in Fig. 1(e), the direct bandgap  $E_g^D$  and indirect one  $E_g^I$  can be estimated from the extrapolation of linear region of  $(\alpha h\nu)^2$  and  $(\alpha h\nu)^{1/2}$  as a function of photon energy  $h\nu$  to zero. Here,  $\alpha$  is the absorption coefficient calculated from optical transmission spectra of the samples according to the Beer-Lambert law. The obtained values of  $E_g^D$  and  $E_g^I$  for  $\text{Pd}_3\text{P}_2\text{S}_8$  are 2.03 and 1.86 eV, in agreement with the values reported previously ( $E_g^D = 2.08$  eV and  $E_g^I = 1.85$  eV) [38]. Both  $E_g^D$  and  $E_g^I$  of  $\text{Pd}_3\text{P}_2(\text{S}_{1-x}\text{Se}_x)_8$  decrease monotonically with increasing  $x$  [Fig. 1(f)]. This is in line with the

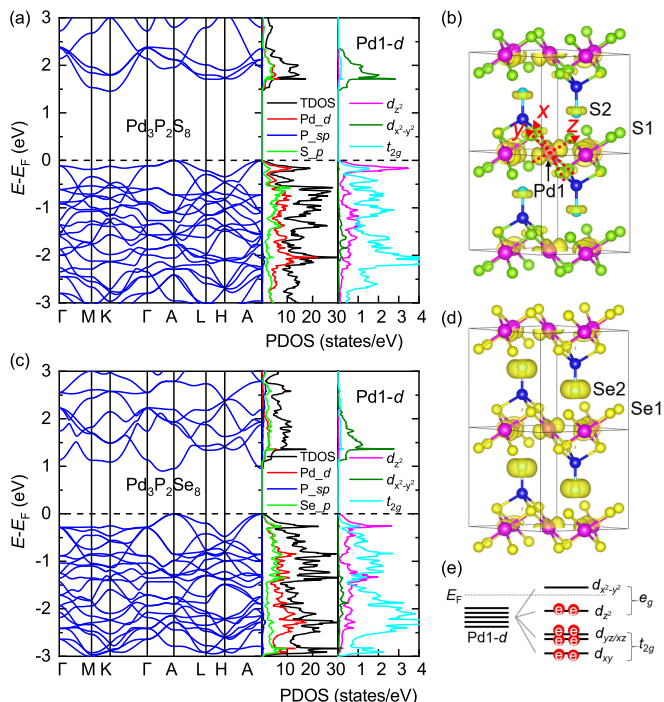


FIG. 2. Band structures, total density of states (TDOS), and PDOS of Pd- $d$ , P- $sp$ , and S(Se)- $p$  orbitals for bulk (a)  $\text{Pd}_3\text{P}_2\text{S}_8$  and (c)  $\text{Pd}_3\text{P}_2\text{Se}_8$ . (b) and (d) The ICDs of flat bands for bulk  $\text{Pd}_3\text{P}_2\text{S}_8$  and  $\text{Pd}_3\text{P}_2\text{Se}_8$ , respectively. The isosurface of charge densities is set to  $0.003 \text{ e}/\text{\AA}^3$ . The local Cartesian coordinates with the origin at the Pd1 atom is defined by the red arrows in (c), where the  $z$ -axis is perpendicular to the  $\text{PdS}_4$  square plane. (e) Schematic diagram of crystal field splitting for the Pd1 atom.

color changes of single crystals from red orange to dark red with Se doping.

Theoretical calculations confirm the increased lattice parameters and decreased bandgaps of  $\text{Pd}_3\text{P}_2(\text{S}_{1-x}\text{Se}_x)_8$  with Se doping [see Table S1 in Supplemental Material (SM)] [41]. To mimic the structure of  $\text{Pd}_3\text{P}_2(\text{S}_{0.75}\text{Se}_{0.25})_8$ , two typical structural configurations namely P-1 with Se atoms at S1 site (P-1 phase) and P-2 with Se atoms at S2 site (P-2 phase) are considered (Fig. S1 in SM) [41]. The calculated total energy of the P-1 phase are  $363.2 \text{ meV/f.u.}$  lower than that of the P-2 phase for  $\text{Pd}_3\text{P}_2(\text{S}_{0.75}\text{Se}_{0.25})_8$ . It indicates that Se atoms prefer to dope into the S1 site, which may result from the longer bond length and weaker binding strength of the P-S1 bond than those of the P-S2 bond. The calculated lattice parameters of hypothetical  $\text{Pd}_3\text{P}_2\text{Se}_8$  are larger than those of  $\text{Pd}_3\text{P}_2\text{S}_8$  due to the larger ionic radius of  $\text{Se}^{2-}$  than  $\text{S}^{2-}$ . Meanwhile, the theoretical value of  $E_g^I$  of  $\text{Pd}_3\text{P}_2\text{Se}_8$  is also smaller than that of  $\text{Pd}_3\text{P}_2\text{S}_8$  [41], consistent with the experimental trend [Fig. 1(d)].

In order to understand the evolutions of bandgap and FB of  $\text{Pd}_3\text{P}_2(\text{S}_{1-x}\text{Se}_x)_8$  with Se doping, we first study the electronic structures of bulk  $\text{Pd}_3\text{P}_2\text{S}_8$ . Even with the three-dimensional structural features and the contribu-

tions of multiple orbitals from Pd, P, and S atoms, some of the unique features of the 2D kagome lattice of Pd still can be observed in  $\text{Pd}_3\text{P}_2\text{S}_8$ , including the FB centered just below the Fermi level  $E_F$  and the Dirac point at the  $K$  point of Brillouin zone [Fig. 2(a)]. From the partial density of states (PDOS), it can be seen that the valance bands near the  $E_F$  mainly consist of Pd- $d$  and S- $p$  orbitals, while the P orbitals are far away from the  $E_F$ . The common peaks of Pd- $d$  and S- $p$  PDOSs indicate the presence of  $p$ - $d$  hybridizations. These  $p$ - $d$  hybridizations varied for influence and dominance below  $-0.28 \text{ eV}$ , while for the FBs, it mainly depends on Pd- $d$  orbitals. In comparison with other kagome materials,  $\text{Pd}_3\text{P}_2\text{S}_8$  has a FB with rather small bandwidth. To explore its origin, we calculate the integrated charge densities (ICDs) of FBs for bulk  $\text{Pd}_3\text{P}_2\text{S}_8$  with the local Cartesian coordinates, whose axes are along the Pd-S bonds and perpendicular to the  $\text{PdS}_4$  square plane [Fig. 2(b)]. Interestingly, the FB exhibits a nearly single-orbital (Pd- $d_{z^2}$ -like orbital) behavior with the direction perpendicular to the  $\text{PdS}_4$  square plane. Actually, this can be well explained by the splitting of energy level of  $\text{Pd}^{2+}$  ion in the local square-planar crystal field [Fig. 2(e)], similar to the case of  $\text{NdNiO}_2$  [53]. The topmost occupied orbital of  $\text{Pd}^{2+}$  ion is  $d_{z^2}$  and this is consistent with the PDOS shown in Fig. 2(a). In addition, the bands just below the FB are mainly consist of Pd- $t_{2g}$  (nondegenerate  $d_{xy}$  and doubly degenerate  $d_{yz}/d_{xz}$ ) orbitals and S- $p$  orbitals [Fig. 2(a)]. This  $p$ - $d$  hybridization results in the large dispersion of these bands. In contrast, because of the large distance between the Pd atom and the S2 atoms in the neighboring layers, the electron hopping perpendicular to the  $\text{PdS}_4$  square plane is limited and there is only small amount of charges around S2 atoms contributing to the FB [Fig. 2(b)], giving rise to the small bandwidth of FB. In fact, similar phenomenon is also observed at the surface of the kagome metal  $\text{FeSn}$  by destructing electronic hopping along the vertical direction [54].

Considering Se doping, the main features of electronic structure of bulk  $\text{Pd}_3\text{P}_2(\text{S}_{1-x}\text{Se}_x)_8$  ( $x = 0.25$  and  $1$ ) [Figs. 2(c) and S2 in SM] are similar to that of  $\text{Pd}_3\text{P}_2\text{S}_8$  [41]. But the weight of Se- $p$  orbitals below the  $E_F$  in  $\text{Pd}_3\text{P}_2\text{Se}_8$  is larger than that of S- $p$  orbitals in  $\text{Pd}_3\text{P}_2\text{S}_8$  [Figs. 2(a) and 2(c)], suggesting the stronger  $p$ - $d$  hybridizations in the former. Meanwhile, the dispersions of FB and the ICDs around Se2 in  $\text{Pd}_3\text{P}_2\text{Se}_8$  are also larger than those of  $\text{Pd}_3\text{P}_2\text{S}_8$  [Figs. 2(b) and 2(d)]. Furthermore, the FB of P-2 phase exhibits a larger dispersion along the  $\Gamma$ -A direction than that of P-1 phase [Fig. S2 in SM] [41]. This large dispersion can also partially explain the reduced  $E_g^I$  with Se doping, especially at S2 site [Fig. 1(f) and Table S1 in SM] [41]. Above results clearly indicate that with increasing Se content the increase of Pd-Ch (Ch = S, Se)  $p$ - $d$  hybridization, especially when the Se atoms locate at apical sites, has a significant influence on interlayer coupling, dispersion of

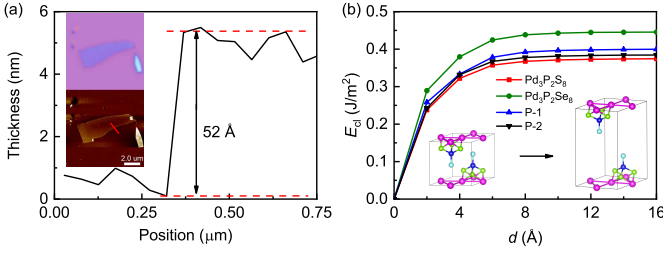


FIG. 3. (a) Height profile across sample edge along the direction shown by the arrow in the lower inset. Upper and lower insets show the optical and AFM images of a cleaved thin flake of  $\text{Pd}_3\text{P}_2\text{S}_8$  crystal. The bar in lower inset is  $2\ \mu\text{m}$ . (b) Calculated  $E_{\text{cl}}$  as a function of  $d$  for  $\text{Pd}_3\text{P}_2\text{S}_8$ ,  $\text{Pd}_3\text{P}_2\text{Se}_8$ , as well as  $\text{Pd}_3\text{P}_2(\text{S}_{0.75}\text{Se}_{0.25})_8$  with P-1 and P-2 configurations.

FB and bandgap, which seems to be a disadvantage to realize the ultra-FB of Pd kagome lattice.

In order to reduce the interlayer coupling, a natural idea is to exfoliate the layered compounds of  $\text{Pd}_3\text{P}_2\text{Ch}_8$  down to monolayers. Previous experiment reported that  $\text{Pd}_3\text{P}_2\text{S}_8$  can be easily cleaved down to few layers or even monolayer [38]. For the whole series of  $\text{Pd}_3\text{P}_2\text{Ch}_8$  crystals, they are also easy to exfoliate to few layers like  $\text{Pd}_3\text{P}_2\text{S}_8$ . Here, we take  $\text{Pd}_3\text{P}_2\text{S}_8$  as an example for cleavage. The step height across an edge of the cleaved sample [red line in the lower inset of Fig. 3(a)] is  $52\ \text{\AA}$  [Fig. 3(a)], which is about 7 unit cells of  $\text{Pd}_3\text{P}_2\text{S}_8$ . Moreover, the rather large area of exfoliated thin flake with the same color ( $\sim 7 \times 3\ \mu\text{m}^2$ ) suggests a uniform thickness through the whole sample [upper inset of Fig. 3(a)]. It is noted that the thin flakes of  $\text{Pd}_3\text{P}_2\text{Ch}_8$  are stable in air without color change for several days. To reveal the evolution of interlayer coupling strength with Se doping further, the cleavage energies  $E_{\text{cl}}$  are calculated by increasing interlayer distance  $d$  [inset of Fig. 3(b)]. The  $E_{\text{cl}}$  increases quickly with increasing  $d$  and then converges to the saturation value of  $0.37\ \text{J/m}^2$  ( $23\ \text{meV/\AA}^2$ ) when  $d$  is larger than  $\sim 8\ \text{\AA}$ . With Se doping, the  $E_{\text{cl}}$  increases gradually and reaches  $0.45\ \text{J/m}^2$  ( $28\ \text{meV/\AA}^2$ ) for hypothetical  $\text{Pd}_3\text{P}_2\text{Se}_8$ . In addition, the P-1 phase has a slightly larger  $E_{\text{cl}} = 0.40\ \text{J/m}^2$  than the P-2 phase ( $E_{\text{cl}} \sim 0.38\ \text{J/m}^2$ ). These results confirm the significant influence of chalcogen atoms at apical site on the strength of interlayer coupling. Although the  $E_{\text{cl}}$  increases with Se doping, they are still comparable with those values for most of the well-known vdW materials, like graphite and  $\text{MoS}_2$  ( $E_{\text{cl}} = 13 - 21\ \text{meV/\AA}^2$ ) [51]. Thus  $\text{Pd}_3\text{P}_2\text{Ch}_8$  can be classified to the group of easily exfoliable materials ( $E_{\text{cl}} < 35\ \text{meV/\AA}^2$ ) [52], even they have the wavy structure of Pd-P-Ch layers.

The feasible cleavage of  $\text{Pd}_3\text{P}_2\text{Ch}_8$  down to atomically thin films or even monolayer alters the interlayer coupling and also has a significant influence on its electronic structure. To further clarify the evolution of FBs with the strength of interlayer interaction, we consider the con-

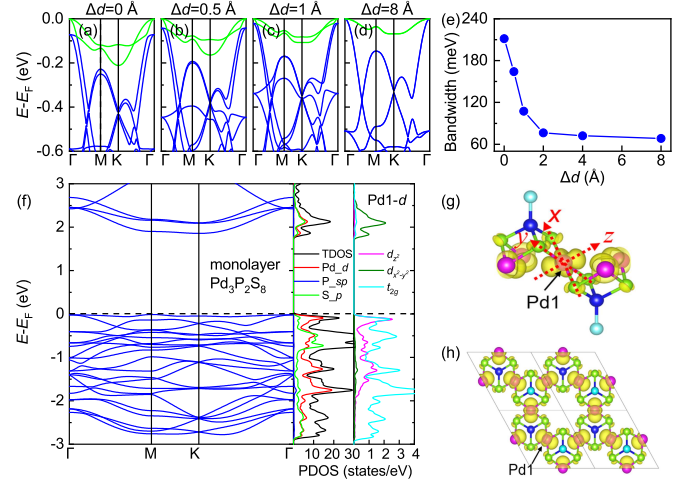


FIG. 4. (a)-(d) Band structures of the bilayer  $\text{Pd}_3\text{P}_2\text{S}_8$  with increasing  $\Delta d$ . The green bands mark the two FBs. (e) The bandwidth of two FBs as a function of  $\Delta d$ . (f) Band structure, TDOS, and PDOS of Pd- $d$ , P- $sp$ , and S- $p$  orbitals for monolayer  $\text{Pd}_3\text{P}_2\text{S}_8$ . (g) Side view and (h) top view of the ICDs of FB for the monolayer  $\text{Pd}_3\text{P}_2\text{S}_8$ .

tinuous evolution of band structure in bilayers  $\text{Pd}_3\text{P}_2\text{S}_8$  with the variation of interlayer spacing  $\Delta d = (d - d_{\text{bulk}})$ , where  $d_{\text{bulk}}$  is the interlayer distance in bulk materials [Fig. 4(a)]. When the  $\Delta d = 0$ , the strong interlayer interaction leads to the coupling of two sets of FBs derived from two different layers with relatively large bandwidth. With increasing  $\Delta d$ , the weakened coupling of two sets of FBs narrows the bandwidth [Figs. 4(b) and 4(c)]. Finally when the  $\Delta d$  is large enough ( $\Delta d = 8\ \text{\AA}$ ), the interlayer coupling becomes negligible and the two sets of FBs are almost degenerated [Fig. 4(d)]. Correspondingly, the bandwidth of two FBs decreases by more than threefold [Fig. 4(e)]. If exfoliated to monolayer, the Pd-S2 distance becomes infinite and the charge around S2 atoms vanishes [Figs. 4(g) and 4(h)], suggesting the lack of interlayer electron hopping along the out-of-plane direction. As a result, the much narrower bandwidth of FB ( $\sim 68\ \text{meV}$ ) appears in the monolayer of  $\text{Pd}_3\text{P}_2\text{S}_8$  [Figs. 4(f)]. On the other hand, the bandwidth of FB for monolayer  $\text{Pd}_3\text{P}_2\text{Se}_8$  is slightly larger than that of monolayer  $\text{Pd}_3\text{P}_2\text{S}_8$  and the ICDs near Se1 is also larger than that of S1 in  $\text{Pd}_3\text{P}_2\text{S}_8$  [Figs. S3 in SM] [41]. It suggests that the increased intralayer coupling between Pd and Se1 due to stronger  $p$ - $d$  hybridization are also unfavorable for the flatness of FB.

In summary, we study the doping effects of Se on the vdW kagome semiconductor  $\text{Pd}_3\text{P}_2\text{S}_8$  single crystals. It is found that with Se doping the lattice parameters increase but the bandgaps  $E_g$  decrease monotonically, which be related to the increased dispersion of FB near  $E_F$  due to the enhanced interlayer coupling due to Se doping, especially when Se atoms occupy the apical sites of  $\text{PCh}_4$  tetrahedra. In contrast, once such interlayer

coupling is eliminated in monolayer  $\text{Pd}_3\text{P}_2\text{Ch}_8$ , an unusual ultra-FB of Pd kagome lattice with narrow band width can be formed. This ultra-FB not only roots in the kagome structure of  $\text{Pd}_3\text{P}_2\text{Ch}_8$  but also is closely related to the unique square planar crystal field of  $\text{PdCh}_4$  with  $\text{Pd}^{2+}$  ion in  $4d^8$  configuration. The latter one isolates the  $d_{z^2}$  band of from other  $d$  bands of  $\text{Pd}^{2+}$  ion when the interlayer electron hopping perpendicular to the  $\text{PdCh}_4$  square plane is suppressed in the 2D limit. Thus,  $\text{Pd}_3\text{P}_2\text{Ch}_8$  provides a unique platform to study the physics of FB in kagome lattice.

This work was supported by National Key R&D Program of China (Grants No. 2018YFE0202600, No. 2017YFA0302903, and No. 2019YFA0308603), Beijing Natural Science Foundation (Grant No. Z200005), National Natural Science Foundation of China (Grants No. 11822412, No. 11774423, No. 12174443, and No. 11934020), the Fundamental Research Funds for the Central Universities and Research Funds of Renmin University of China (RUC) (Grants No. 18XNLG14, No. 19XNLG13, and No. 19XNLG17), and Beijing National Laboratory for Condensed Matter Physics. Computational resources were provided by the Physical Laboratory of High-Performance Computing at Renmin University of China.

† S.H.Y and B.C.G. contributed equally to this work.

\* Corresponding authors: xfliu@zju.edu.cn (X. F. Liu); kliu@ruc.edu.cn (K. Liu); hlei@ruc.edu.cn (H. C. Lei).

- 
- [1] D. Leykam, A. Andreanov, and S. Flach, *Adv. Phys. X* **3**, 1473052 (2018).
- [2] J.-W. Rhim and B.-J. Yang, *Adv. Phys. X* **6**, 1901606 (2021).
- [3] Z. Liu, F. Liu, and Y.-S. Wu, *Chin. Phys. B* **23**, 077308 (2014).
- [4] A. Mielke, *J. Phys. A: Math. Gen.* **24**, 3311 (1991).
- [5] H. Tasaki, *Prog. Theor. Phys.* **99**, 489 (1998).
- [6] S. Miyahara, S. Kusuta, and N. Furukawa, *Physica C* **460**, 1145 (2007).
- [7] W.-H. Ko, P. A. Lee, and X.-G. Wen, *Phys. Rev. B* **79**, 214502 (2009).
- [8] C. Wu, D. Bergman, L. Balents, and S. Das Sarma, *Phys. Rev. Lett.* **99**, 070401 (2007).
- [9] B. Jaworowski, A. D. Güçlü, P. Kaczmarkiewicz, M. Kupczyński, P. Potasz, and A. Wójs, *New J. Phys.* **20**, 063023 (2018).
- [10] K. Ohgushi, S. Murakami, and N. Nagaosa, *Phys. Rev. B* **62**, R6065 (2000).
- [11] E. Tang, J.-W. Mei, and X.-G. Wen, *Phys. Rev. Lett.* **106**, 236802 (2011).
- [12] A. Mielke, *J. Phys. A: Math. Gen.* **24**, L73 (1991).
- [13] A. Mielke, *J. Phys. A: Math. Gen.* **25**, 4335 (1992).
- [14] B. Sutherland, *Phys. Rev. B* **34**, 5208(1986).
- [15] E. H. Lieb, *Phys. Rev. Lett.* **62**, 1201 (1989).
- [16] H. Tasaki, *Phys. Rev. Lett.* **69**, 1608 (1992).
- [17] C. Wu and S. D. Sarma, *Phys. Rev. B* **77**, 235107 (2008).
- [18] Z. Liu, Z. F. Wang, J. W. Mei, Y. S. Wu, and F. Liu, *Phys. Rev. Lett.* **110**, 106804 (2013).
- [19] S.-L. Yu and J.-X. Li, *Phys. Rev. B* **85**, 144402 (2012).
- [20] W.-S. Wang, Z.-Z. Li, Y.-Y. Xiang, and Q.-H. Wang, *Phys. Rev. B* **87**, 115135 (2013).
- [21] M. L. Kiesel, C. Platt, and R. Thomale, *Phys. Rev. Lett.* **110**, 126405 (2013).
- [22] L. Balents, *Nature* **464**, 199 (2010).
- [23] L. Ye, M. Kang, J. Liu, F. von Cube, C. R. Wicker, T. Suzuki, C. Jozwiak, A. Bostwick, E. Rotenberg, D. C. Bell, L. Fu, R. Comin, J. G. Checkelsky, *Nature* **555**, 638 (2018).
- [24] Z. Lin, J.-H. Choi, Q. Zhang, W. Qin, S. Yi, P. Wang, L. Li, Y. Wang, H. Zhang, Z. Sun, L. Wei, S. Zhang, T. Guo, Q. Lu, J.-H. Cho, C. Zeng, and Z. Zhang *Phys. Rev. Lett.* **121**, 096401 (2018).
- [25] Z. Liu, M. Li, Q. Wang, G. Wang, C. Wen, K. Jiang, X. Lu, S. Yan, Y. Huang, D. Shen, J.-X. Yin, Z. Wang, Z. Yin, H. Lei, and S. Wang, *Nat. Commun.* **11**, 4002 (2020).
- [26] M. Kang, S. Fang, L. Ye, H. C. Po, J. Denlinger, C. Jozwiak, A. Bostwick, E. Rotenberg, E. Kaxiras, J. G. Checkelsky, and R. Comin, *Nat. Commun.* **11**, 4004 (2020).
- [27] M. Li, Q. Wang, G. Wang, Z. Yuan, W. Song, R. Lou, Z. Liu, Y. Huang, Z. Liu, H. Lei, Z. Yin, and S. Wang, *Nat. Commun.* **12**, 3129 (2021).
- [28] T.-H. Han, J. S. Helton, S. Chu, D. G. Nocera, J. A. Rodriguez-Rivera, C. Broholm, and Y. S. Lee, *Nature* **492**, 406 (2012).
- [29] S. Nakatsuji, N. Kiyohara, and T. Higo, *Nature* **527**, 212 (2015).
- [30] E. Liu, Y. Sun, N. Kumar, L. Muechler, A. Sun, L. Jiao, S.-Y. Yang, D. Liu, A. Liang, Q. Xu, J. Kroder, V. Stüf, H. Borrmann, C. Shekhar, Z. Wang, C. Xi, W. Wang, W. Schnelle, S. Wirth, Y. Chen, S. T. B. Goennenwein, and C. Felser, *Nat. Phys.* **14**, 1125 (2018).
- [31] Q. Wang, Y. Xu, R. Lou, Z. Liu, M. Li, Y. Huang, D. Shen, H. Weng, S. Wang, and H. Lei, *Nat. Commun.* **9**, 3681 (2018).
- [32] J.-X. Yin, S. S. Zhang, H. Li, K. Jiang, G. Chang, B. Zhang, B. Lian, C. Xiang, I. Belopolski, H. Zheng, T. A. Cochran, S.-Y. Xu, G. Bian, K. Liu, T.-R. Chang, H. Lin, Z.-Y. Lu, Z. Wang, S. Jia, W. Wang, and M. Z. Hasan, *Nature* **562**, 91 (2018).
- [33] J.-X. Yin, S. S. Zhang, G. Chang, Q. Wang, S. S. Tsirkin, Z. Guguchia, B. Lian, H. Zhou, K. Jiang, I. Belopolski, N. Shumiya, D. Multer, M. Litskevich, T. A. Cochran, H. Lin, Z. Wang, T. Neupert, S. Jia, H. Lei, and M. Z. Hasan, *Nat. Phys.* **15**, 443 (2019).
- [34] J.-X. Yin, W. Ma, T. A. Cochran, X. Xu, S. S. Zhang, H.-J. Tien, N. Shumiya, G. Cheng, K. Jiang, B. Lian, Z. Song, G. Chang, I. Belopolski, D. Multer, M. Litskevich, Z.-J. Cheng, X. P. Yang, B. Swidler, H. Zhou, H. Lin, T. Neupert, Z. Wang, N. Yao, T.-R. Chang, S. Jia, and M. Z. Hasan, *Nature* **583**, 533 (2020).
- [35] B. R. Ortiz, S. M. L. Teicher, Y. Hu, J. L. Zuo, P. M. Sarte, E. C. Schueller, A. M. M. Abeykoon, M. J. Krogstad, S. Rosenkranz, R. Osborn, R. Seshadri, L. Balents, J. He, and S. D. Wilson, *Phys. Rev. Lett.* **125**, 247002 (2020).
- [36] B. R. Ortiz, P. M. Sarte, E. Kenney, M. J. Graf, S. M. L. Teicher, R. Seshadri, and S. D. Wilson, *Phys. Rev. Mater.* **5**, 034801 (2021).

- [37] Q. Yin, Z. Tu, C. Gong, Y. Fu, S. Yan, and H. Lei, *Chin. Phys. Lett.* **38**, 037403 (2021).
- [38] S. Park, S. Kang, H. Kim, K. H. Lee, P. Kim, S. Sim, N. Lee, B. Karuppannan, J. Kim, J. Kim, K. I. Sim, M. J. Coak, Y. Noda, C.-H. Park, J. H. Kim, and J.-G. Park, *Sci. Rep.* **10**, 20998 (2020).
- [39] T. A. Bither, P. C. Donohue, and H. S. Young, *J. Solid State Chem.* **3**, 300 (1971).
- [40] A. Simon, K. Peters, E. M. Peters, and H. Hahn, *Z. Naturforsch. B* **38**, 426 (1983).
- [41] See Supplemental Material for the detailed methods of crystal growth, experimental characterizations and theoretical calculations, the theoretical crystal structure of  $\text{Pd}_3\text{P}_2(\text{S}_{0.75}\text{Se}_{0.25})_8$ , the band structures, TDOS and PDOS of Pd-*d*, P-*sp*, and S-*p* orbitals for bulk and monolayer  $\text{Pd}_3\text{P}_2(\text{S}_{0.75}\text{Se}_{0.25})_8$  with P-1 and P-2 configurations and  $\text{Pd}_3\text{P}_2\text{Ch}_8$ , which includes Refs. [42–49].
- [42] P. E. Blöchl, *Phys. Rev. B* **50**, 17953 (1994).
- [43] G. Kresse and D. Joubert, *Phys. Rev. B* **59**, 1758 (1999).
- [44] G. Kresse and J. Hafner, *Phys. Rev. B* **47**, 558 (1993).
- [45] G. Kresse and J. Furthmüller, *Comput. Mater. Sci.* **6**, 15 (1996).
- [46] G. Kresse and J. Furthmüller, *Phys. Rev. B* **54**, 11169 (1996).
- [47] J. P. Perdew, K. Burke, and M. Ernzerhof, *Phys. Rev. Lett.* **77**, 3865 (1996).
- [48] S. Grimme, J. Antony, S. Ehrlich, and S. Krieg, *J. Chem. Phys.* **132**, 154104 (2010).
- [49] J. P. Perdew, A. Ruzsinszky, J. Tao, V. N. Staroverov, G. E. Scuseria, and G. I. Csonka, *J. Chem. Phys.* **123**, 062201 (2005).
- [50] J. Tauc, R. Grigorovici, and A. Vancu, *Phys. Status Solidi B* **15**, 627 (1966).
- [51] T. Björkman, A. Gulans, A. V. Krasheninnikov, and R. M. Nieminen, *Phys. Rev. Lett.* **108**, 235502 (2012).
- [52] N. Mounet, M. Gibertini, P. Schwaller, D. Campi, A. Merkys, A. Marrazzo, T. Sohier, I. E. Castelli, A. Cepellotti, G. Pizzi, and N. Marzari, *Nat. Nano.* **13**, 246 (2018).
- [53] P. Jiang, L. Si, Z. Liao, and Z. Zhong, *Phys. Rev. B* **100**, 201106(R) (2019).
- [54] M. Han, H. Inoue, S. Fang, C. John, L. Ye, M. K. Chan, D. Graf, T. Suzuki, M. P. Ghimire, W. J. Cho, E. Kaxiras, and J. G. Checkelsky, *Nat. Commun* **12**, 5345 (2021).